SIMULATIONS AND DESIGN OF A PROTOTYPE RESISTIVE PLATE CHAMBER

by

Emre Burak Yıldızcı

B.S., Physics, Boğaziçi University, 2017

Submitted to the Institute for Graduate Studies in
Science and Engineering in partial fulfillment of
the requirements for the degree of
Master of Science

Graduate Program in Physics

Boğaziçi University

2021

ACKNOWLEDGEMENTS

I would like to express my gratitude to my supervisor Prof. Erkcan Özcan for his guidance and support throughout my graduate studies and beyond. He has inspired me to become an experimental physicist.

I would like to extend my appreciation to my parents Aysel and Bekir Yıldızcı for always supporting me and my sister Elanur Yıldızcı for always being there for me.

I am also grateful to my grandfather Abdülkadir Ayhan, my uncle Ziver Ayhan and my cousin Furkan Ayhan for providing me with encouragement to get through this period.

I also thank TÜBİTAK for financially supporting me through 2210-E National Scholarship Programme for MSc Students.

ABSTRACT

SIMULATIONS AND DESIGN OF A PROTOTYPE RESISTIVE PLATE CHAMBER

Resistive Plate Chambers (RPCs) are particle detectors used by a wide variety of experiments around the world to cover large detection areas as they have good spatial and time resolutions as well as an uncomplicated construction process and are relatively inexpensive. A domestic prototype RPC has been built at KAHVELab and promising preliminary results have been acquired. In this thesis, various aspects of RPC design have been simulated and the results, which are in agreement with the literature, are presented. In addition, basics of muography, an imaging method based on atmospheric muons, are discussed and simulations have been performed for various detection setups both with ideal detectors, to gauge the limitations, and RPCs with varying spatial resolutions. The results suggest that RPCs, even with modest spatial resolutions, can be utilized in absorption muography.

ÖZET

PROTOTİP DİRENÇLİ PLAKA ODASI DİZAYNI VE BENZETİMİ

Dirençli Plaka Odaları (DiPlO'lar), iyi konum ve zaman çözünürlüğüne ve karmaşık olmayan üretim sürecine sahip oldukları ve görece olarak ucuz oldukları için, dünyanın birçok yerindeki çok çeşitli deneylerde büyük algılama alanlarını kaplamak için kullanılmaktadır. KAHVELab'da yerel bir prototip DiPlO üretilmiş olup ümit verici öncü sonuçlar elde edilmiştir. Bu tezde, DiPlO dizaynının bir çok yönü benzetime sokulmuş, literatürle örtüşen sonuçlar elde edilmiş ve bu sonuçlar sunulmuştur. Ek olarak, atmosferik müonlara dayanan bir görüntüleme tekniği olan müografinin temel öğeleri tartışılmış, sınırlamaları ölçmek adına ideal dedektörlerle ve bununla beraber konum çözünürlüğü değişen DiPlO'larla çeşitli algılama düzenekleri için benzetimler gerçekleştirilmiştir. Elde edilen sonuçlar mütevazı konum çözünürlüğüne sahip DiPlO'ların dahi soğurulum müografisinde kullanılabileceğini göstermektedir.

TABLE OF CONTENTS

LIST OF FIGURES

LIST OF TABLES

LIST OF SYMBOLS

A	Mass number
Ar	Argon
c	Speed of light
$C_2H_2F_4$	Tetrafluoroethane
CO_2	Carbon dioxide
d	Electrode thickness
d_0	Distance vertical muons travel
d_θ	Distance non-vertical muons travel
E	Energy
$E_{binding}$	Binding energy
E_{code}	Energy value in code
E_f	Final energy
E^γ	Power law for cosmic ray energy
E_i	Initial energy
E_{kin}	Kinetic Energy
$E(r)$	Electric field at r
E_{table}	Energy value in table
E_w	Weighting field
g	Gas gap thickness
h	height
$\hbar\omega$	Energy of the incident photon
$\hbar\omega'$	Energy of the scattered photon
I	Mean excitation energy
I_{ind}	Induced current
$\mathrm{i}-C_4H_{10}$	Isobutane
L	Thickness
M	Particle mass
m_e	Electron mass

m_μ	Muon mass
N	Density of atoms
n	Index of refraction
n_0	Number of initial electrons
N_{down}	Muon flux through the downstream pair
n_e	Number of total electrons
N_{up}	Muon flux through the upstream pair
P	Momentum
Q_{tot}	Total charge
q	Charge
R	Radius
r	Distance from the symmetry axis
SF_6	Sulfur hexafluoride
T_{max}	Maximum energy transfer to the electron
v	Velocity
v_d	Drift velocity
X_0	Radiation length
Z	Atomic number
α	First Townsend coefficient
γ	Lorentz factor
$\delta(\beta)$	Density-dependent correction term
ϵ_0	Vacuum permittivity
ϵ_r	Relative dielectric permittivity of the electrode
Θ	Scattering angle
θ	Angle
λ	Mean free path
ρ	Density
σ	Cross section
σ_p	Surface charge density

LIST OF ACRONYMS/ABBREVIATIONS

ATLAS	A Toroidal LHC Apparatus
AM	Absorption muography
CMS	Compact Muon Solenoid
EM	Electromagnetic
Geant4	Geometry and Tracking
HEED	High Energy Electro-Dynamics
HV	High voltage
KAHVELab	Kandilli Detector, Accelerator and Instrumentation Laboratory
LHC	Large Hadron Collider
Mu2e	Muon-to-Electron-Conversion Experiment
OPERA	Oscillation Project with Emulsion-tRacking Apparatus
pdf	probability density function
rms	root mean square
RPC	Resistive Plate Chamber
SM	Scattering Muography

1. INTRODUCTION

There are various subatomic particles that have been playing crucial roles in the development of particle physics due to their abundance in nature such as electrons, protons and photons. However, abundance is not the only criteria that makes a particle experimentally favored. Muon, another subatomic particle, has a combination of properties, most notably lifetime and mass, that make it one of the focal interests of experiments that sit on the opposite ends of the particle physics experiment spectrum in terms of their luminosity, as in the case of experiments with very high luminosity such as ATLAS and CMS and rare event experiments such as Mu2e, or in terms of their source, as in the case of experiments with earth-based and cosmic accelerators. Muons are elementary particles classified as charged leptons, together with electrons and tau particles, by the Standard Model. Mass of a muon (105.7 MeV/c^2) is about 200 times that of an electron (0.5 MeV/c^2). This mass difference allows muons to penetrate longer distances and serves as the main differentiator between otherwise two very similar particles in detection point of view.

The importance of muons in experimental particle physics has drawn attention to the research and development studies of detectors specialized in muon detection. In addition, the aforementioned experimental variety requires different type of detectors dedicated to the varying needs of experiments. As an example, for high luminosity experiments, rate capability is crucial while for muon tomography experiments portability is the key element. Resistive Plate Chambers (RPCs) are gaseous detectors that offer great time resolution and good spatial resolution. There are different RPC designs, e.g. single gap, double gap, timing and so on, that cover a wide range of experimental needs. They are used in general-purpose experiments such as ATLAS and CMS at Large Hadron Collider (LHC), neutrino oscillation experiments, e.g. OPERA, DAYA BAY, luminosity frontier experiments like those at the B factories and many other experiments.

Due to their versatility and relatively low-cost production process, RPCs are among the ideal detectors to have the pioneering study started in a region where the native experimental high energy community has recently been developing. Aligning with this goal, a prototype RPC has been produced at KAHVELab [1], a particle physics research laboratory at Boğaziçi University. As a follow-up work, in this thesis, simulation studies have been performed testing the design parameters of RPCs as well as their performance in muon tomography.

In the subsequent sections, first, theoretical introduction to the particle interactions in matter as well as Cosmic Rays are presented. Then, detection principles and various simulation results of RPCs are discussed. Later, muography and its simulations with different detector setups are introduced.

2. PARTICLE INTERACTIONS IN MATTER

Particle detectors rely on the interaction of particles in matter. As opposed to the deterministic nature of classical physics, quantum theory, which is used to describe the physics of subatomic particles, has a probabilistic nature. There are various key concepts that need to be defined before the different particle interaction types are introduced.

2.1. Cross-section and Mean Free Path

When a particle travels inside a material, at the microscopic level, the probability of an interaction $dp(x)$ is proportional to the distance traveled dx and the number density of atoms (or nuclei) N. The proportionality constant depends both on the properties of the material (atomic number Z and mass number A) and the energy E of the particle [2]. Therefore one can define the cross section with

$$dp(x) = dx\ N\ \sigma(E, Z, A). \tag{2.1}$$

This is the same statistics as the particle decay process where the probability of decay at any time is proportional to the time interval. Therefore, the particle interaction in matter is also a Poisson process in position domain and similar to the mean lifetime one can define the mean free path as

$$\begin{aligned} P(x) &= e^{-xN\sigma} = e^{-\frac{x}{\lambda}} \\ \lambda &= \frac{1}{N\sigma}\ . \end{aligned} \tag{2.2}$$

In the case of a mixture material, above definition of the mean free path becomes [2]

$$\lambda = \frac{1}{\sum N_i \sigma_i} \ . \tag{2.3}$$

2.2. Interactions of Charged Particles in Matter

2.2.1. Ionization and Excitation

When a charged particle is near an atom it can interact with the electrons or the nucleus of the atom through the Coulomb force. If the charged particle collides with an electron, the electron can, depending on the transferred energy and the energy levels of the atom, either be liberated (ionization) or transferred to a higher energy level (excitation).

The energy loss of a charged particle in matter where ionization is the dominant source, is given by the Bethe-Bloch formula [3]

$$\frac{dE}{dx} = \rho \frac{Z}{A} (0.307 \text{ MeV cm}^2/\text{g}) \frac{1}{\beta^2} \left[\frac{1}{2} ln \left(\frac{2 m_e c^2 \beta^2 \gamma^2 T_{max}}{I^2} \right) - \beta^2 - \frac{\delta(\beta)}{2} \right] \tag{2.4}$$

where ρ is the density, Z and A are the atomic and mass number of the material respectively, m_e is the electron mass, c is the speed of light, $\beta = v/c$, $\gamma = E/m$ of the charged particle, T_{max} is the maximum energy transfer to the electron, I is the mean excitation energy and $\delta(\beta)$ is the density-dependent correction term.

Since the mass of a charged particle, other than the electron itself and positron, is much larger than the mass of an electron, due to these collisions the trajectory of the charged particle remains unchanged to a very good approximation.

2.2.2. Multiple Scattering

If a charged particle collides with the nucleus of an atom, and especially if it is much lighter than the nucleus, it will not lose a significant amount of energy but instead, its direction will be changed. This effect is called multiple scattering and the

root mean square (rms) deviation of the scattering angle in three dimensions when the particle penetrates a thickness L in matter is given by [3]

$$\sqrt{\langle \Theta^2 \rangle} = \frac{Z}{Pc\beta}(20 \text{ MeV})\sqrt{\frac{L}{X_0}} \tag{2.5}$$

where P is the momentum of the particle and X_0 is the matter dependent radiation length, which is approximately 300 m for dry air [4].

2.2.3. Cherenkov Radiation

When a charged particle with velocity v travels in a medium of index of refraction n, faster than the speed of light in that medium c/n, a light is emitted at a certain angle with respect to the direction of the charged particle that satisfies

$$\cos(\theta_c) = \frac{c}{nv} \ . \tag{2.6}$$

This effect is called the Cherenkov radiation and is illustrated in Figure 2.1.

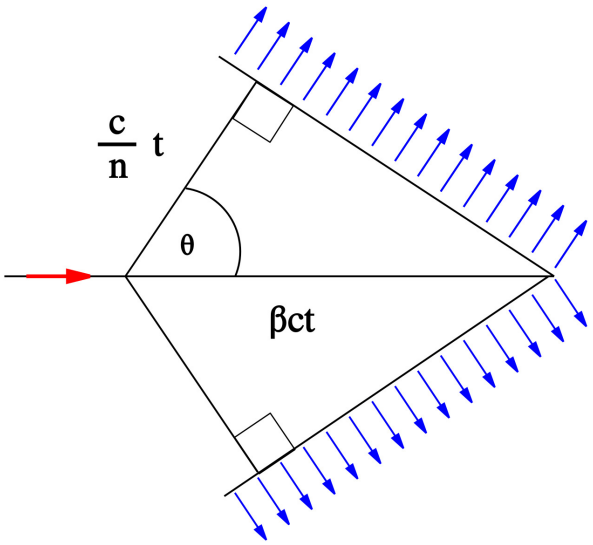

Figure 2.1. Cherenkov cone of a particle traveling with a speed greater than c/n.

2.2.4. Bremsstrahlung

When a charged particle collides with a nucleus, its direction is changed, hence, it undergoes acceleration and emits photons. The directions of the emitted photons will have a spectrum that is strongly peaked in the original direction of the charged particle. The average energy loss of electrons due to bremsstrahlung is given by

$$\frac{dE}{dx} = -\frac{E}{X_0} \ . \tag{2.7}$$

The energy loss due to bremsstrahlung for particles other than an electron or positron is suppressed by $(m_e/M)^2$ factor where M is the particle mass [3]. Therefore this effect is relevant at very high energies for heavy particles.

2.2.5. Overview of Interactions of Muons in Matter

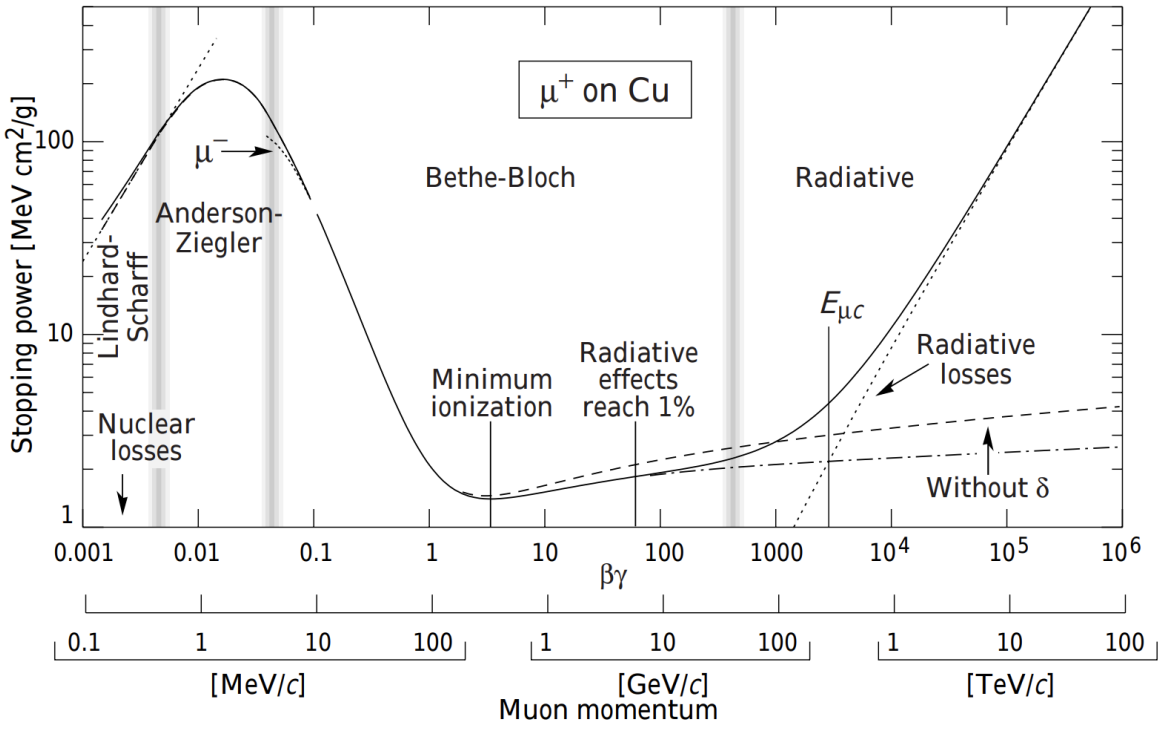

Figure 2.2. Stopping power for positive muons in copper between momentum values 100 keV/c and 100 TeV/c. Reprinted from [4].

Although the momentum ranges where the interaction mechanisms dominate differs for different materials that the muons are traveling in, the order remains the same. Stopping power in copper for positive muons as a function of muon momentum is illustrated in Figure 2.2.

2.2.6. Photoelectric Effect

In the photoelectric process, a photon is absorbed by an atom and its energy is transferred to a bound electron of the atom. Depending on the energy of the photon and which electron the energy is transferred to, the photoelectric process can yield either a liberated electron or an excited atom. In the most likely case, the energy is transferred to a K shell electron and the kinetic energy of the liberated electron E_{kin} is given by

$$E_{kin} = \hbar\omega - E_{binding} \tag{2.8}$$

where $E_{binding}$ is the binding energy of the atom and $\hbar\omega$ is the energy of the incident photon.

2.3. Interaction of Photons in Matter

2.3.1. Compton Scattering

When a photon interacts with an electron elastically, some of its energy is transferred to the electron and to conserve the energy and momentum the direction of the incident photon also changes. Assuming a free electron, the energy of the scattered photon $\hbar\omega'$, as a function of the scattering angle θ, is

$$\hbar\omega' = \frac{\hbar\omega}{\frac{\hbar\omega}{m_e c^2}(1 - \cos(\theta)) + 1} \ . \tag{2.9}$$

2.3.2. Pair Production

Pair production is the process where a photon is annihilated and an electron positron pair is created. This process only occurs if the photon energy is greater than the total mass of the final state, which is two times the mass of an electron, and if the photon is in the presence of the Coulomb field of a nucleus in order to conserve the energy and momentum.

3. COSMIC RAYS AND AIR SHOWERS

Cosmic rays are particles, mostly protons and alpha particles with some fraction of heavier nuclei, that originate from outside of our solar system. These particles, upon entering the Earth's atmosphere, collide with the nuclei in air, lose about half of their energy and produce many secondary hadrons, mainly charged and neutral pions. Neutral pions, since they have a very short lifetime (8.43×10^{-17} s [4]) compared to charged pions, decay without further interactions and produce 2 photons as shown in

$$\pi^0 \rightarrow 2\gamma. \tag{3.1}$$

These photons initiate the electromagnetic (EM) shower component of the air shower (Figure 3.1).

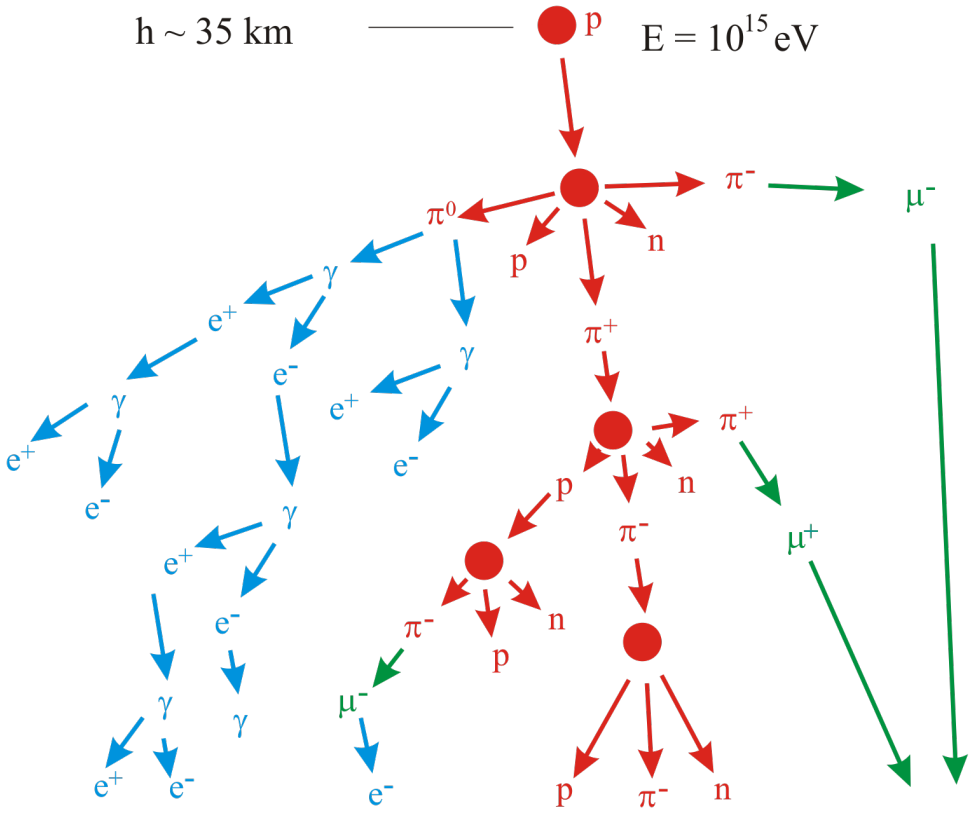

Figure 3.1. Development of an air shower initiated by a proton.

Charged pions (and kaons) interact with the air molecules and produce secondary mesons. This cascade process continues until the charged pions and kaons decay dominantly into muons as shown below

$$\begin{aligned} \pi^+ &\to \mu^+ \nu_\mu \qquad & \pi^- &\to \mu^- \bar{\nu}_\mu \\ K^+ &\to \mu^+ \nu_\mu \qquad & K^- &\to \mu^- \bar{\nu}_\mu . \end{aligned} \tag{3.2}$$

Since the bremsstrahlung process is suppressed by a factor of $(m_e/m_\mu)^2$ for muons, as discussed earlier, these atmospheric muons lose energy mainly via ionization and propagate through the atmosphere and, as they have a relatively long lifetime (2.2×10^{-6} s [4]), reach the Earth.

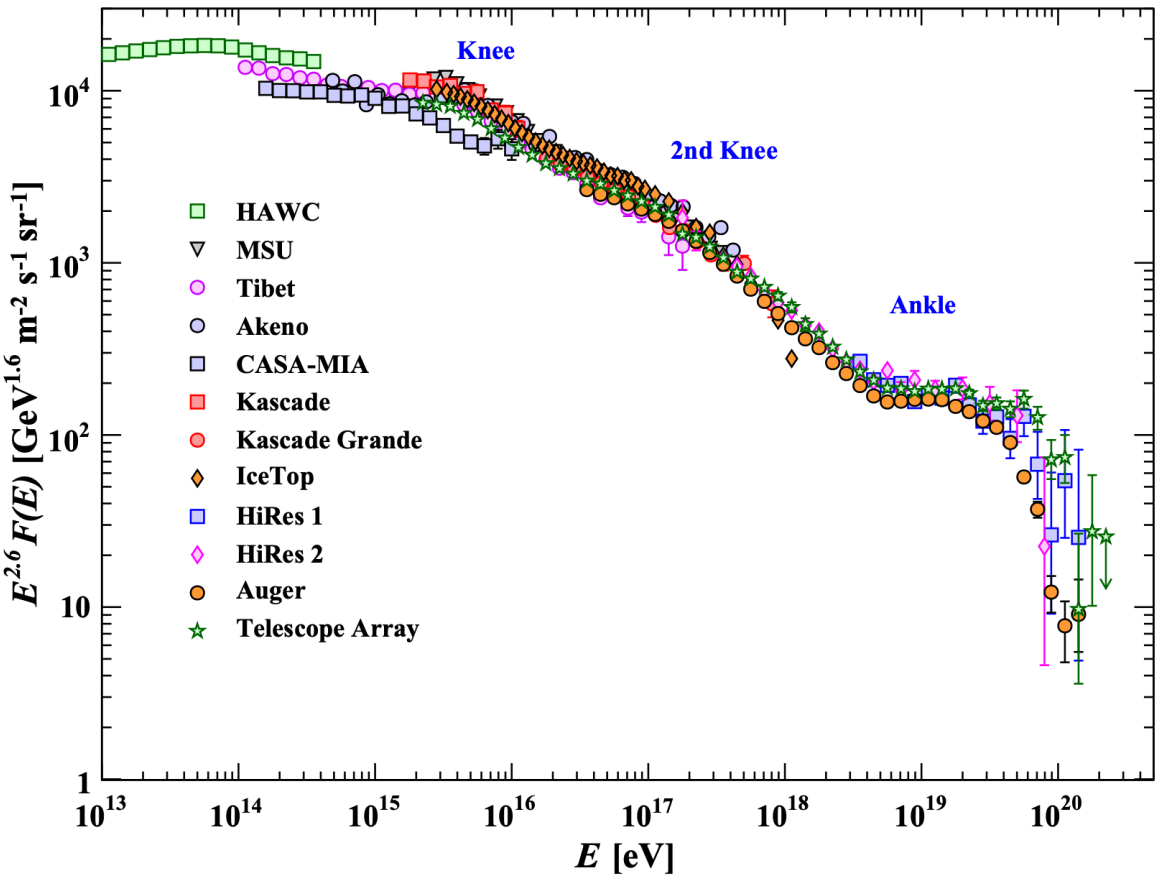

Figure 3.2. Energy spectrum of cosmic rays. Reprinted from [4].

3.1. Atmospheric Muon Flux

The energy dependence of the atmospheric muon flux stems from three main reasons: the energies of cosmic rays, the energies of the parent mesons, and the distance they travel in the atmosphere before reaching the Earth. Figure 3.2 shows the energy distribution of cosmic rays that follows the power law E^{γ}, where $\gamma \sim 2.7$ with some deviations at very high energies [3].

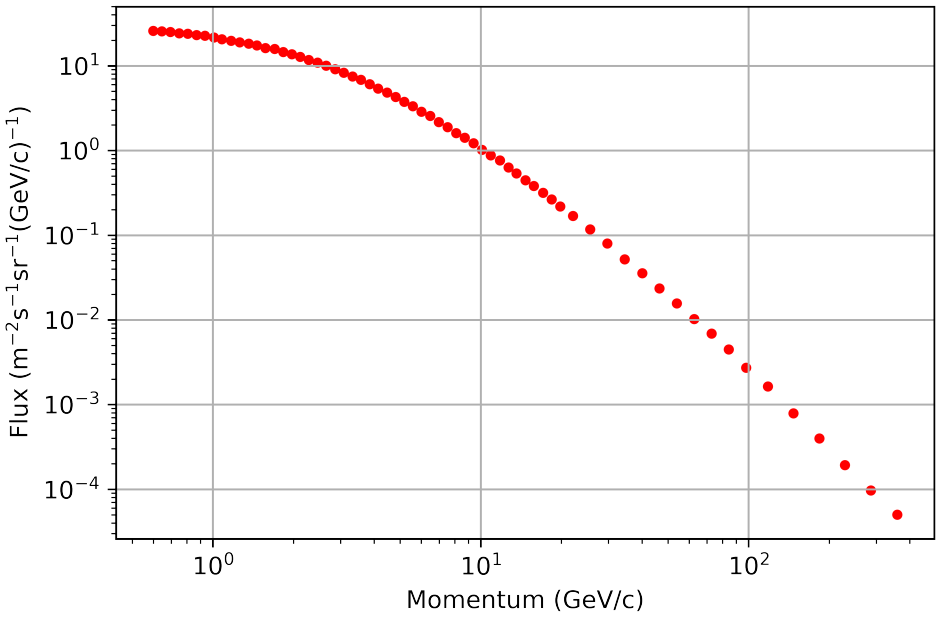

Figure 3.3. Atmospheric muon energy spectrum. The data are obtained at KEK in Tsukuba, Japan in 2002 [5].

Since the distance muons travel in the atmosphere is directly related to the altitude and the zenith angle, the momentum distribution is given at fixed altitude and zenith angle. Figure 3.3 shows an example distribution with the data obtained in Tsukuba, Japan in 2002 [5]. Altitude dependence can easily be understood as the muons lose energy due to ionization as they penetrate through the atmosphere. Location dependence comes mainly from the Earth's magnetic field as the cosmic ray penetration is more difficult near the equator than the poles [6].

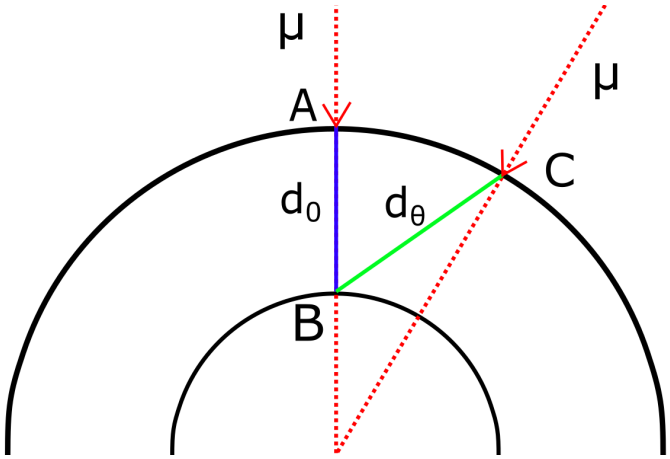

Figure 3.4. Illustration of the pathlength dependence on the zenith angle. Points A and C are the production points for two muons. Assuming a detector at point B, a vertical muon travels distance d_0 to reach the detector while a muon with zenith angle θ travels distance d_θ.

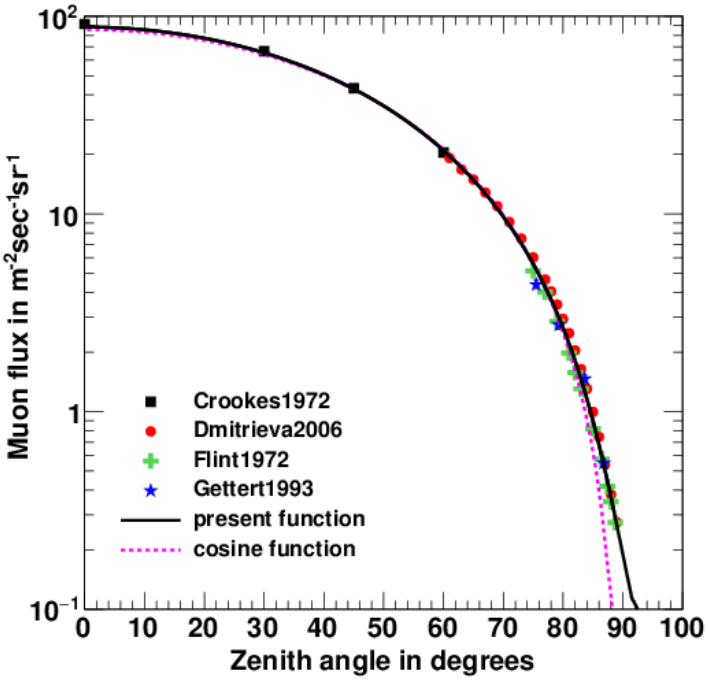

Figure 3.5. Atmospheric muon zenith angle spectrum. Present function is proportional to $(d_\theta/d_0)^{-2}$ and cosine function is its flat earth approximation version, $\cos^2(\theta)$. Reprinted from [6].

As a result of the difference between the pathlengths of muons with different zenith angles (as illustrated in Figure 3.4) the flux per solid angle decreases as the zenith angle increases (Figure 3.5). The flux of muons at zenith angle θ is proportional to $(d_\theta/d_0)^{-(n-1)}$, where d_θ and d_0 is shown in Figure 3.4 and $n \approx 3$ [6]. The flat earth approximation, which is invalid for higher zenith angles, simplifies the ratio of d_θ/d_0 to $\cos^{-1}(\theta)$.

4. RESISTIVE PLATE CHAMBERS

Muons play a key role for both cosmic ray experiments, and experiments with man-made accelerators. One of the detectors that offers a good time and spatial resolution and capable of operating at high rates is the RPC. In the subsequent sections, first, the working principle of RPCs will be introduced, then the design considerations of a typical RPC will be discussed and finally, various simulation toolkits will be reviewed and simulation results will be presented.

4.1. Basics of RPC Working Principle

4.1.1. Overview of RPC design

Schematic layout of a typical RPC is shown in Figure 4.1. The components and the brief descriptions of their functionalities from center to outside are given in the following sections.

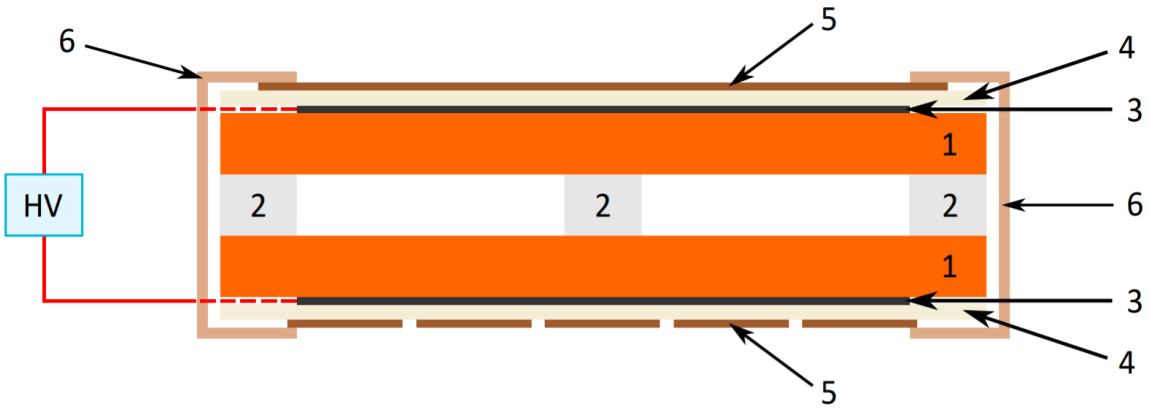

Figure 4.1. Schematic of an RPC. 1- Resistive electrodes, 2- Spacers, 3- Semiconductive layers, 4- Insulating sheets, 5- Readout strips, 6- Insulating tapes. Reprinted from [1].

4.1.1.1. Gas Gap. Gas gap is the active region of the detector where primary ionization and signal development occurs. Gas composition is mainly chosen so that it provides the required number of primary ionizations as well as the localization of the signal.

4.1.1.2. Spacers. Spacers seal the gas gap and ensure its uniformity, hence allowing a uniform electric field required for RPC operation.

4.1.1.3. Resistive Electrodes. RPCs use resistive electrodes, as opposed to metallic plates used by their precursors, which leads to an indirect signal development mechanism. This new design equips RPCs with an internal discharge quenching mechanism [7].

4.1.1.4. Semiconductive Layers. High voltage (HV) is applied through the semiconductive layer, which is typically a graphite paint. The resistivity is tuned such that the semiconductive layer spreads the HV uniformly and is transparent to the induced signals.

4.1.1.5. Insulating Sheets. The insulation between the semiconductive layer, hence the applied HV, and the readout strips is vital for the detector operation.

4.1.1.6. Readout Strips. The signal is read through the readout strips that are placed on both sides of the detector. The adjacent strips are parallel to each other while the strips that are on the opposite sides of the detector are perpendicular to provide a two-dimensional position measurement.

4.1.1.7. Insulating Tapes. The rigidity of the whole detector and its insulation are secured by the insulating tapes.

4.1.2. Primary Ionization in Gaseous Media

Although sharing the same mechanism, ionization in gaseous media can be classified by the initiating particles, i.e. muons and electrons. Here, ionization due to the primary muon will be discussed. As introduced earlier, the main energy loss mechanism of muons at energies relevant for most of the particle physics experiments is ionization and the formula governing it is the Bethe-Bloch formula (Equation (2.4)). However, the Bethe-Bloch formula is valid for the mean energy loss and stochastic fluctuations must be taken into account especially for thin layers. For detectors with moderate thicknesses, such as RPCs and scintillators, this effect can be described to a certain degree by the Landau distribution [4].

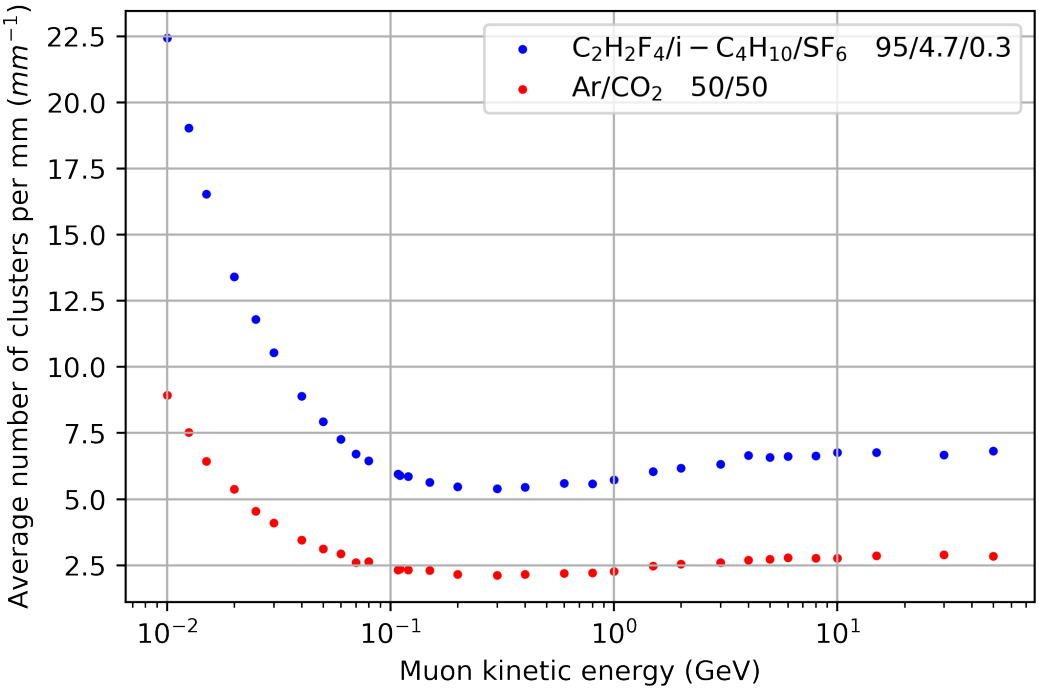

Figure 4.2. Simulation results of average number of clusters per mm as a function of muon energy for a gas composition typically used by RPCs and for another composition more commercially available and can be used for preliminary RPC tests.

One of the parameters that deviates from the mean is the number of electron-ion clusters per mm along the trajectory of the primary muon. In Figure 4.2, average

numbers of clusters per mm as a function of muon energy are shown for two different gas compositions as simulated by HEED [8]. In Figure 4.3, for a fixed muon kinetic energy of 4 GeV, probability distribution of clusters/mm is given for the same gas compositions.

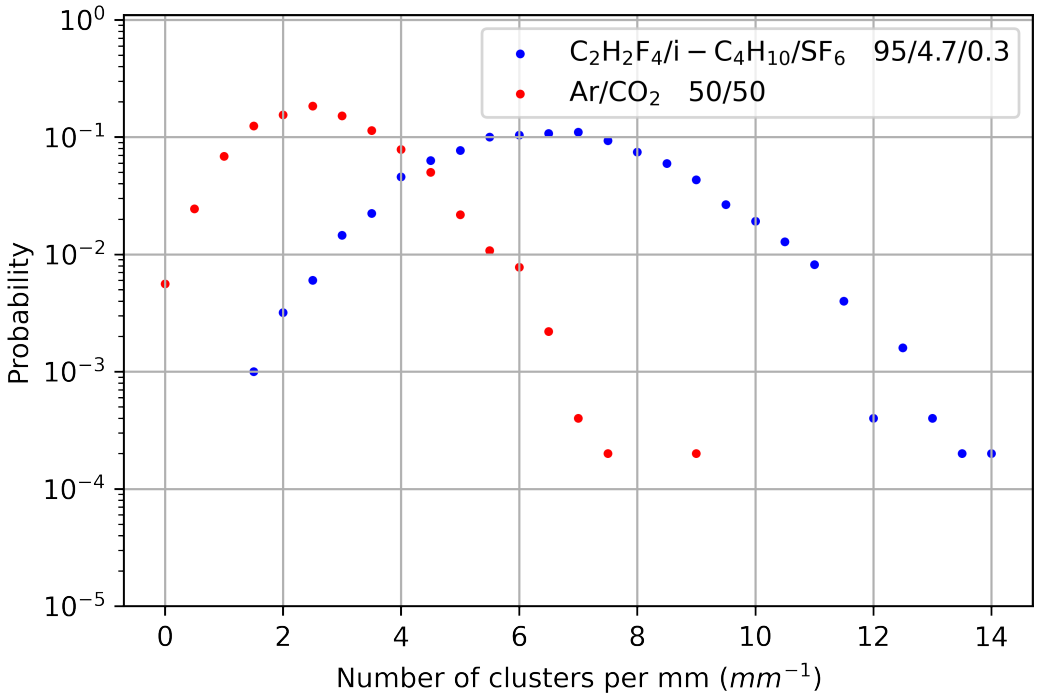

Figure 4.3. Probability density function of number of clusters per mm for a fixed muon kinetic energy of 4 GeV for two different gas compositions as simulated by Garfield++.

One of the implications of this deviation is that it imposes a limitation on the intrinsic efficiency of RPCs as there should be enough number of primary clusters produced within a certain distance from the cathode for the development of electron avalanches.

4.1.3. Electron Avalanche in Gaseous Media

As the signal in an RPC is induced by the charges moving inside the gas gap, understanding how charges transport in gaseous media plays a key role in designing

RPCs. Here, electron movement will be considered first and the main differences between ion and electron transports will be discussed.

When an impinging muon liberates an electron, most of the time, the electron has a negligible kinetic energy and without the presence of external electric field it gets absorbed before moving macroscopic distances. When an external field is applied, however, the electron feels a force opposite the electric field and its energy increases until it interacts with an atom. This interaction can either be elastic, i.e. multiple scattering, that leaves the energy of the electron almost unchanged, due to the large mass difference between the electron and atom, but direction deviated, or inelastic, where it collides with another electron bound to an atom and transfers some of its energy, that either excites the atom or liberates another electron as discussed earlier. The increase in the number of free electrons is proportional to the current number and this yields an exponential growth, i.e. avalanche, as [7]

$$\begin{aligned} dn_e &= \alpha n_e dx \\ n_e &= n_0 e^{\alpha \Delta x} \end{aligned} \tag{4.1}$$

where α is known as the first Townsend coefficient, typically in the order of 10 mm^{-1}, n_e is the number of total electrons, and n_0 is the number of initial electrons.

4.1.4. Signal Formation

The signal formation mechanism of RPCs differ from its historical precursors, e.g. ionization chambers, wire chambers, where the charges that are moving inside the active region reach the metallic electrodes and induce a signal, i.e. voltage pulses. In an RPC, however, charges get neutralized when they reach the resistive electrodes and never reach the readout strips. In order to explain how the signal is formed, method of image charges will be introduced for the simplest case of a point charge and a grounded, infinite metallic plate (Figure 4.4), and the induced current on the plate will be computed. Then, the induced current formula will be modified for the parallel

plate geometry.

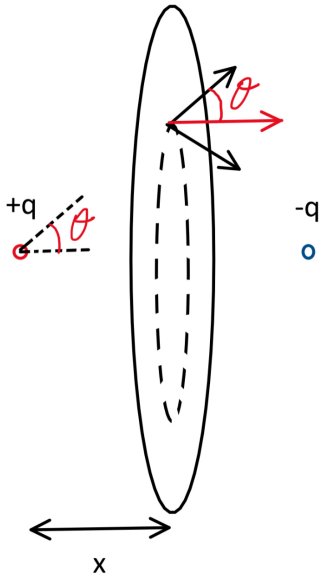

Figure 4.4. Method of image charges illustrated for the simplest case of a single point charge q (on the left) and its image charge $-q$ (on the right). Electric field lines from both the real and the image charge are shown in black. The total electric field is shown in red.

When there is a charge q present in front of a grounded, infinite metallic plate, one can assume an image charge of $-q$ on the other side of the plate to calculate the electric field for the side where the real charge is on. The resulting electric field close to the metallic plate and a distance r away from the symmetry axis, shown with a red arrow in Figure 4.4, can be calculated as

$$\begin{aligned} E(r) &= \frac{q}{4\pi\epsilon_0(x^2+r^2)}\ \cos(\theta) + \frac{q}{4\pi\epsilon_0(x^2+r^2)}\ \cos(-\theta) \\ &= \frac{qx}{2\pi\epsilon_0(x^2+r^2)^{3/2}}\ . \end{aligned} \tag{4.2}$$

Then, using Gauss's law, surface charge density σ_p can be obtained as

$$\begin{aligned} E(r) &= -\frac{\sigma_p}{\epsilon_0} = \frac{qx}{2\pi\epsilon_0(x^2+r^2)^{3/2}} \\ \sigma_p &= -\frac{qx}{2\pi(x^2+r^2)^{3/2}}\ . \end{aligned} \tag{4.3}$$

One has to omit the 1/2 factor in the Gauss's Law as there is no electric field on the imaginary charge's side.

This surface charge density can be used to compute the charge accumulated on a disk-shaped area with radius R as

$$\begin{aligned} Q_{tot} &= \int_0^R \sigma_p dA = \int_0^R \sigma_p 2\pi r dr = -\int_0^R \frac{qx2\pi r}{2\pi(x^2+r^2)^{3/2}} dr \\ Q_{tot} &= \frac{qx}{(x^2+r^2)^{1/2}}\Big|_0^R = q\left(\frac{x}{(x^2+R^2)^{1/2}} - 1\right). \end{aligned} \tag{4.4}$$

The parameter relevant for the readout signal, induced current (I_{ind}), is the time derivative of this charge, which can be calculated as

$$\begin{aligned} I_{ind} = \frac{dQ_{tot}}{dt} &= q\left(\frac{\dot{x}}{(x^2+R^2)^{1/2}} - \frac{x^2\dot{x}}{(x^2+R^2)^{3/2}}\right) \\ &= \frac{q\dot{x}}{(x^2+R^2)^{1/2}}\left(1 - \frac{x^2}{x^2+R^2}\right) \\ &= \frac{q\dot{x}}{R} = \frac{qv_d}{R} \end{aligned} \tag{4.5}$$

where v_d is the drift velocity of the charge q.

When the parallel plate geometry of the RPCs is considered, there will be an infinite number of image charges instead of one (an image charge of one plate will behave like a real charge for the other plate), which complicates the computation of the induced current but leaves q and v_d terms unchanged. The Shockley-Ramo theorem [7] states that the induced current expression for any geometry can simply be expressed as [7]

$$I_{ind} = q\boldsymbol{v_d} \cdot \boldsymbol{E_w} \tag{4.6}$$

by introducing a geometry dependent term "weighting field", E_w. For an RPC, ignoring the edge effects, E_w is given by [7]

$$E_w = \frac{1}{g + 2d/\epsilon_r} \tag{4.7}$$

where g and d are the gas gap and electrode thicknesses respectively and ϵ_r is the relative dielectric permittivity of the electrode.

4.2. Simulation

Simulation plays a crucial role for high energy physics experiments in both the design of the experiments and the analyses of the experimental data. One of the motivations of this thesis is to provide various simulation results of a simple RPC that yield a better understanding of the relevant design parameters. In this section, Monte Carlo method will be introduced as the fundamental mechanism of the different simulation toolkits used. Subsequently, the basics of the toolkits will be discussed. Once the fundamentals are discussed, various simulation results regarding multiple aspects of the RPCs will be presented.

4.2.1. Monte Carlo Methods

Monte Carlo methods are mathematical techniques utilized to predict the outcomes of events that have a probabilistic nature. The basic idea is to use the appropriate repeated random sampling for the probabilistic aspects of the problem and do the relevant computations on the samples to get the outcomes. As an example, a particle penetrating through a medium can be considered. There could be many stochastic energy loss mechanisms relevant depending on the energy and various other parameters of the particle and medium. Using the random sampling and the cross section of each interaction type, energy loss of the particle can be computed. If this process is done enough times, until the desired statistics is acquired, the relevant parameters, such as the average energy loss, can be predicted.

4.2.2. Toolkits

4.2.2.1. Geant4. Geant4 is a widely used toolkit to simulate particle interactions in matter based on Monte Carlo methods [9]. It is used by some of the largest experiments such as ATLAS and CMS at LHC. It allows excellent detector customizability and is capable of simulating interactions in a wide variety of materials. It also has a parameterization feature that lets other simulation toolkits perform the simulations in specified regions, for specified particles.

4.2.2.2. Garfield++. Garfield++ is a toolkit for the simulation of charged particle interactions, specifically ionization, in gases and semiconductors [10]. It is capable of simulating the electron avalanche process and many other ionization based parameters.

4.2.3. Basic Simulation Structure

In the simulations performed, the Geant4 code, version 10.6, was responsible for generating the primary particles and propagating them through the detector until they reach the gas gap. Then, the parameters of the impinging particles are transferred to the Garfield++ code and the simulations inside the gas region are performed there.

4.2.4. Results

4.2.4.1. Cluster Simulations. Two different simulation results for electron-ion clusters per mm were discussed earlier. Here, an additional result will be presented regarding the clusters. In Figure 4.5, the simulation results, performed with 2500 muons, for the number of electrons per cluster distribution for a fixed muon energy of 4 GeV for two gas compositions is shown.

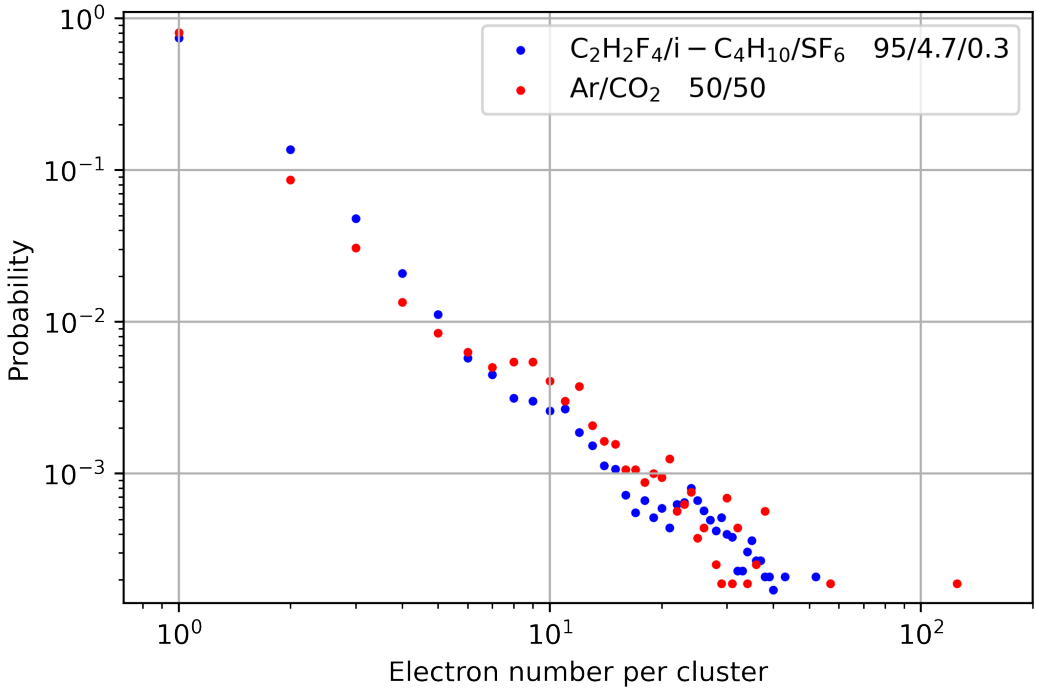

Figure 4.5. Probability density function of number of electrons per cluster for a fixed muon kinetic energy of 4 GeV for two different gas compositions. Obtained with HEED.

4.2.4.2. Efficiency Simulations.

Considerations. First, the electric field across the resistive plates is ignored as it is material dependent and does not play a significant role, shifts the x axis depending on the material permittivity.

Next, Garfield++ is made responsible for the simulation of the active region, gas gap, of the RPC. To simulate the efficiency, one has to set an induced charge, i.e. electron avalanche size, threshold above which the signal can be discriminated from the electronic noise. This threshold strongly depends on the electronic readout system. In order to reduce the computation time, the threshold is initially set to be a very low value of 10 fC. Then additional, low-statistics simulations have been performed to

understand the effect of the threshold value.

Another important simulation remark is the Garfield++ class used to simulate the electron avalanche. Garfield++ offers different classes suitable for different precision and computation time needs. In the simulations performed, "AvalancheMC" class is used to reduce the computation time. Within this class, the step size, the distance particles travel between each simulation step, is set to be 10 μm. This step size is later reduced for additional low-statistics simulations to test the accuracy.

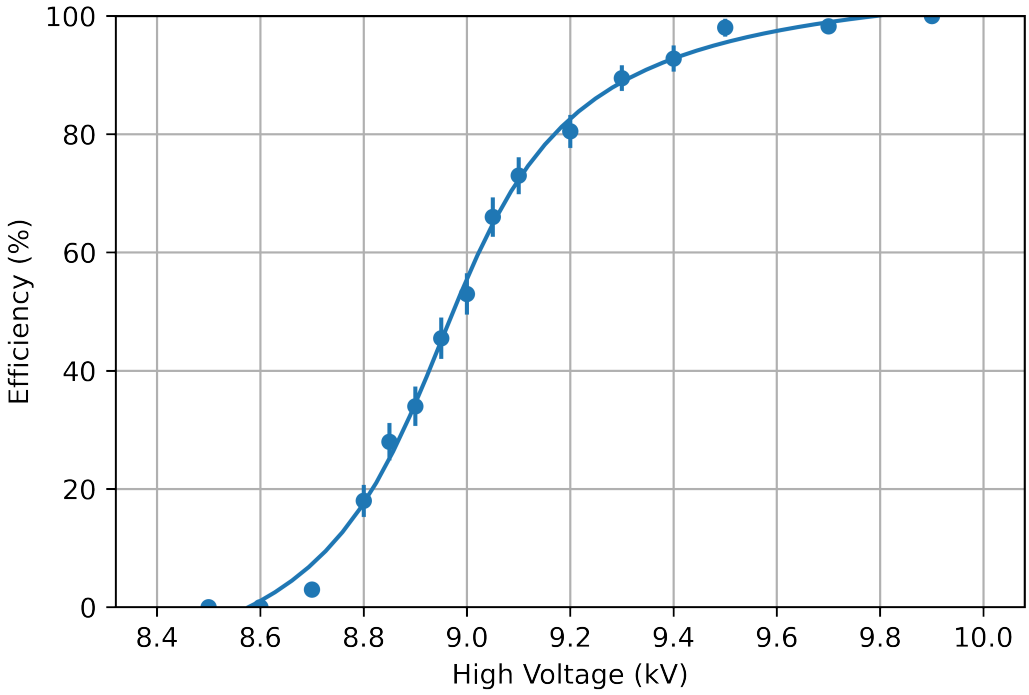

Figure 4.6. Efficiency as a function of operating voltage for RPCs where the charge threshold is 10 fC, simulation step size is 10 μm and gas gap 2 mm.

Results. Figure 4.6 shows the RPC efficiency as a function of the applied HV. This simulation has the highest-statistics but the lowest accuracy and charge threshold. However, it is consistent with the experimental data and simulation results present in the literature [7].

The effect of the simulation step size can be gauged from Figure 4.7, which has been prepared with the step size of 5 μm (half the size of the earlier plots).

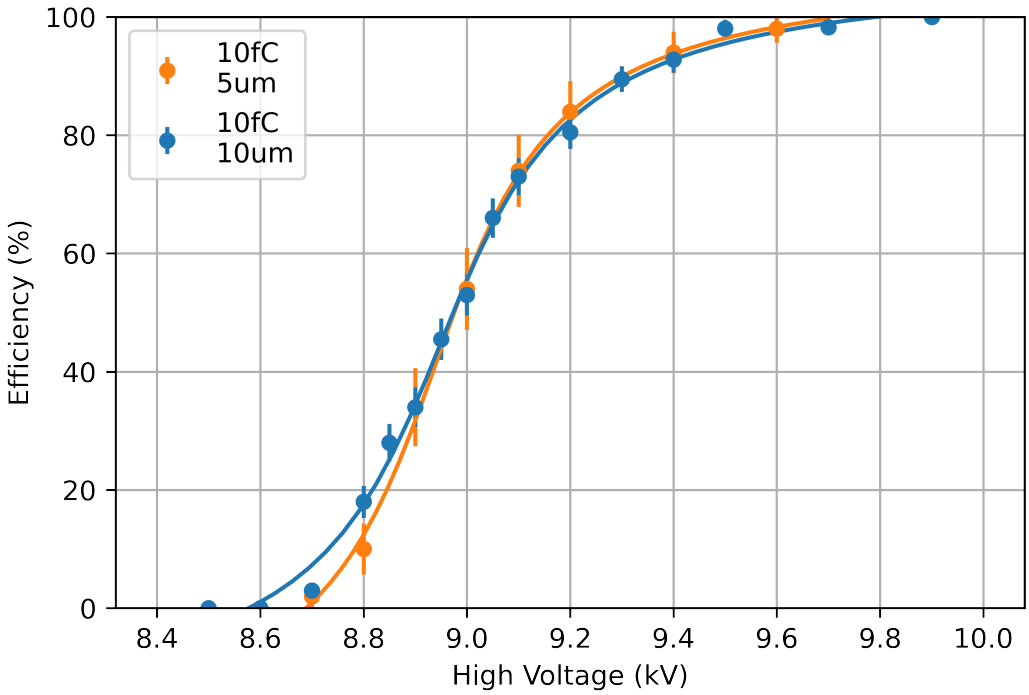

Figure 4.7. Efficiency as a function of operating voltage for RPCs where the charge threshold is 10 fC, simulation step size is 5 μm and 10 μm and gas gap 2 mm.

Figure 4.8 demonstrates the effect of an elevated charge threshold of 50 fC. One can observe the higher voltages required to reach high efficiencies as expected.

Finally, the simulation of a wide gap RPC of gas gap thickness 4mm is performed. Figure 4.9 shows the efficiency as a function of the electric field across the gas gap for thicknesses 4mm and 2mm.

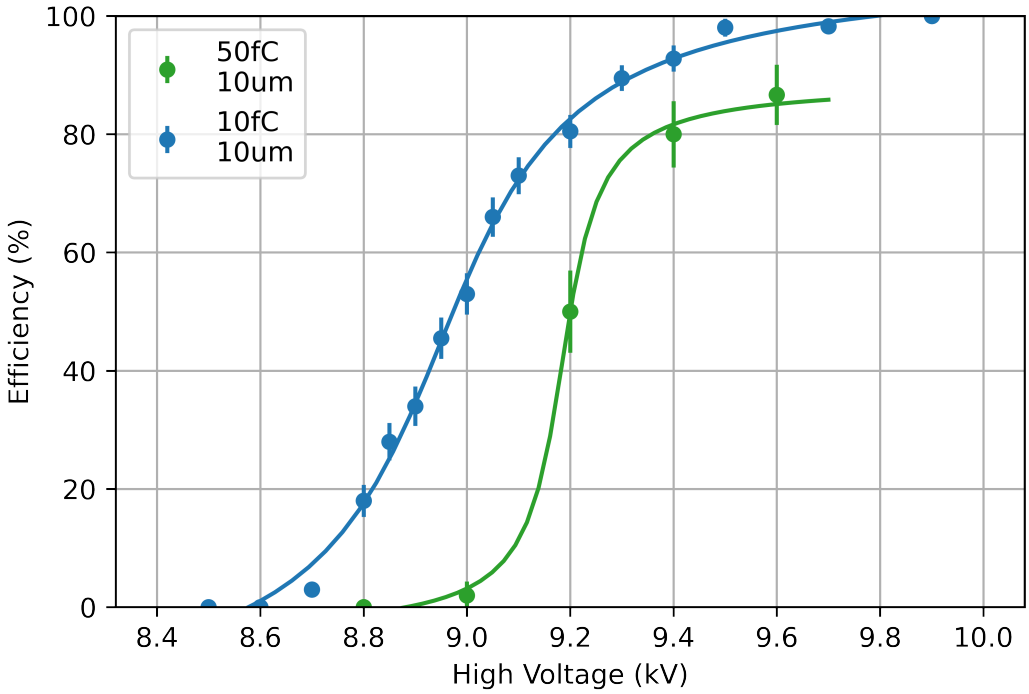

Figure 4.8. Efficiency as a function of operating voltage for RPCs where the charge threshold is 50 fC and 10 fC, simulation step size is 10 μm and gas gap 2 mm.

As both primary ionizations and avalanche processes occur in the gas gap, the distance left for an avalanche to develop depends on the primary ionization position. Therefore, to detect the muons that ionize the gas later in their trajectories, the electric field should be set to a higher value than that is required to detect the muons that ionize the gas immediately as they enter the detector. However, if the electric field is too strong, the avalanches that have the whole gap to grow can lead to spark breakdowns. Hence, wide gap RPCs could be preferable over typical RPCs with gaps 2mm or lower, as they are capable of operating at weaker electric fields as shown in Figure 4.9. A more detailed discussion of the subject, including other considerations, can be found in [11].

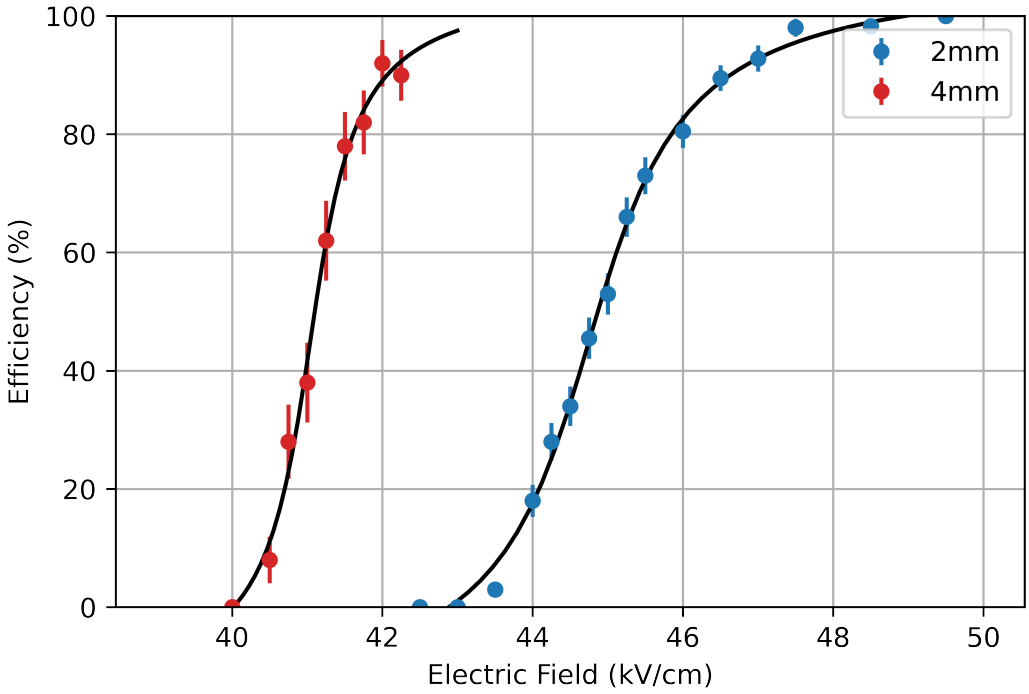

Figure 4.9. Efficiency as a function of electric field in the gas gap for RPCs with gap thicknesses 4mm and 2mm. The charge threshold is 10 fC, simulation step size is 10 μm.

5. MUOGRAPHY

Muography, an imaging method based on atmospheric muons, utilizes the abundant flux of muons with energies near minimum ionizing energy. There are two main techniques, absorption muography (AM), which is based on the attenuation in the muon flux as they traverse a material, and scattering muography (SM), which is based on the direction change of the muons due to multiple scattering inside a material. In the subsequent sections, basic working principle of AM will be presented. Then, various simulation considerations will be discussed. Finally, toy Monte Carlo simulation results for different detector setups will be analyzed.

5.1. Physics of Absorption Muography

As discussed earlier, there are various energy loss mechanisms with relatively distinct energy ranges where they are dominant. For the muons below 10 GeV, the main focus of AM, this mechanism is ionization. According to the Bethe-Bloch equation (Equation (2.4)) total energy loss is proportional to $\int \rho(x)dx$, to a good approximation considering a small energy loss, or simply $\rho \times h$ if the density is uniform. The fraction of muons that cannot reach the other end of the object depends on this column depth. Therefore, if either ρ or h is known the other can be obtained from the attenuation of the flux. This method is powerful for relatively large objects, compared to the size at which SM is efficient, both because the attenuation of the flux increases and fluctuations to the Bethe-Bloch decreases with thickness traversed [4].

5.2. Simulation Considerations

The imaging mechanism depends on the application, hence the detector setup. The general approach is to acquire the downstream, and upstream if possible, flux data experimentally and compare it to a Monte Carlo simulation. Therefore the Monte Carlo simulations play an important role both in designing the experiment and interpreting

the results.

5.2.1. Toy Monte Carlo Simulation for the Energy Spectrum

Energy spectrum is the most important aspect of the muons as it is the main input data regardless of the what the detector setup is. As discussed earlier it depends on various factors and as opposed to various other data it cannot be measured with the AM detectors, hence, it must either be known or estimated carefully.

In the Monte Carlo simulations performed in this thesis, the data presented in [5] and shown in Figure 3.3, which are discrete data but frequent enough at lower energies, are used to create a probability density function for muon energies.

5.2.2. Toy Monte Carlo Simulation for the Angular Spectra

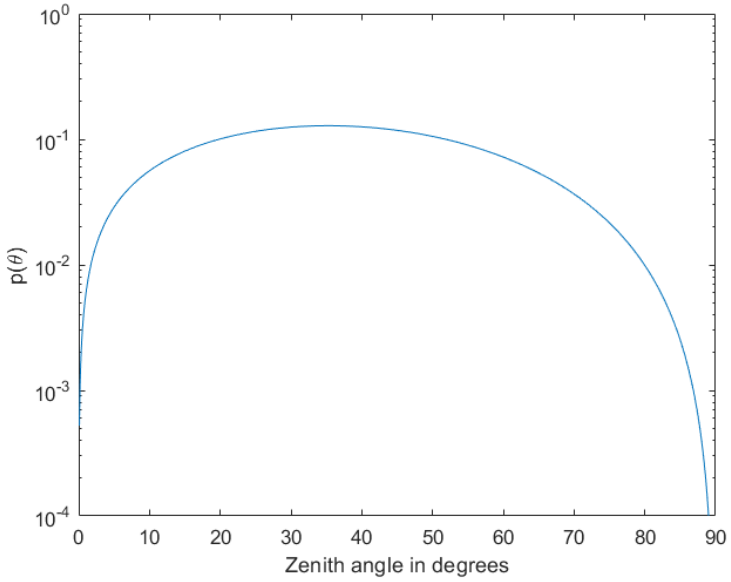

Figure 5.1. Probability density function of the zenith angles of atmospheric muons to be used in the toy Monte Carlo code.

As discussed in [6] and shown in Figure 3.5 the data for the zenith angle spectrum matches almost perfectly, except at large angles above 80° which is not the main focus

of AM, with $\cos^2(\theta)$ function. However, one should be careful as the $\cos^2(\theta)$ function describes the muon flux per solid angle. Therefore to sample the zenith angles of the produced muons, the dependence of the solid angle on the zenith angle, a factor of $\sin(\theta)$, should be considered as well. So the pdf of $\cos^2(\theta)\sin(\theta)$, with the correct normalization factor must be used (Figure 5.1).

The muon flux has a weak azimuthal angle dependence [6] and the Monte Carlo simulation in this study uses a uniform distribution.

5.2.3. Range Calculation as a Function of Energy

Muons in lead (Pb)

Z	A [g/mol]	ρ [g/cm^3]	I [eV]	a	$k = m_s$	x_0	x_1	$\overline{C}$	δ_0
82 (Pb)	207.2(1)	11.350	823.0	0.09359	3.1608	0.3776	3.8073	6.2018	0.14

T	p [MeV/c]	Ionization	Brems	Pair prod	Photonucl	Total	CSDA range [g/cm^2]
		[MeV cm^2/g]					
10.0 MeV	4.704×10^1	3.823				3.823	1.524×10^0
14.0 MeV	5.616×10^1	3.054				3.054	2.705×10^0
20.0 MeV	6.802×10^1	2.436				2.436	4.927×10^0
30.0 MeV	8.509×10^1	1.928				1.928	9.600×10^0
40.0 MeV	1.003×10^2	1.666				1.666	1.521×10^1
80.0 MeV	1.527×10^2	1.283				1.283	4.338×10^1
100. MeV	1.764×10^2	1.215				1.215	5.943×10^1
140. MeV	2.218×10^2	1.151				1.152	9.339×10^1
200. MeV	2.868×10^2	1.124				1.124	1.463×10^2
226. MeV	3.145×10^2	1.122	0.000			1.123	*Minimum ionization*
300. MeV	3.917×10^2	1.130	0.000		0.000	1.131	2.352×10^2
400. MeV	4.945×10^2	1.151	0.000		0.000	1.152	3.228×10^2
800. MeV	8.995×10^2	1.237	0.001		0.000	1.238	6.572×10^2
1.00 GeV	1.101×10^3	1.270	0.001		0.000	1.272	8.165×10^2
1.40 GeV	1.502×10^3	1.322	0.002		0.001	1.325	1.124×10^3
2.00 GeV	2.103×10^3	1.379	0.004	0.001	0.001	1.385	1.567×10^3
3.00 GeV	3.104×10^3	1.442	0.007	0.003	0.001	1.454	2.270×10^3
4.00 GeV	4.104×10^3	1.486	0.010	0.006	0.002	1.504	2.946×10^3
8.00 GeV	8.105×10^3	1.585	0.025	0.022	0.003	1.636	5.486×10^3

Figure 5.2. Various parameters of muons in lead. Reprinted from [12].

The muons that contribute to the imaging calculations are low energy muons where the dominant energy loss mechanism is ionization as discussed earlier. Therefore, the Bethe-Bloch formula (Equation (2.4)) including the density-dependent corrections is used to calculate the range as a function of initial energy for lead, the material chosen for the simulations, as shown below

$$\frac{dE}{dx} = -f(E) \qquad \int_{E_i}^{E_f=0} \frac{dE}{f(E)} = \int_{x_i}^{x_f} dx = \text{range}. \tag{5.1}$$

In order to verify the ranges calculated, the range table for muons in lead (Figure 5.2) is used and consistent results up to a few percent error are acquired.

To improve the range calculations by taking the other energy loss mechanisms into account and to further utilize the data given in the range table, a hybrid approach is employed. In this approach, instead of calculating the range directly using the Bethe-Bloch formula, for an energy value E_{code}, the program finds the closest energy value that the range is known for E_{table} from the table, and depending on whether E_{table} is below or above E_{code}, the code sets E_f or E_i to E_{table} and calculates the distance that must be added to or subtracted from the range given in the table corresponding to E_{table}. The range is calculated by

$$\text{range} = \begin{cases} \text{range from table} + \int_{E_i=E_{code}}^{E_f=E_{table}} \frac{dE}{f(E)} & E_{table} \leq E_{code} \\ \\ \text{range from table} - \int_{E_i=E_{table}}^{E_f=E_{code}} \frac{dE}{f(E)} & E_{code} \leq E_{table}. \end{cases} \tag{5.2}$$

5.3. Simulation Results with Ideal Detectors

In the subsequent sections, simulation results for various detector setups are presented. The detectors used are ideal, i.e. have infinite spatial resolution, therefore, the trajectories of the muons are reconstructed perfectly. This leaves the finite sampling as the only source of error. These results, hence, should be considered as the limits of the AM for the specific setups discussed.

5.3.1. Two-dimensional Imaging with Single Downstream Detector

This setup is the most basic setup that provides a very basic information about the object. There is a single detector placed downstream the object (Figure 5.3) which

only provides flux data as a function of position without any angular information. This serves as a sanity check to see if the code is working.

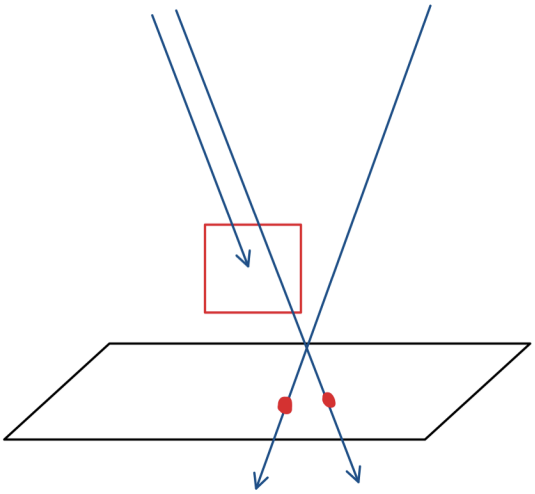

Figure 5.3. Detector setup 1

A setup with a cubical lead block of side length 100 cm placed at the center of a square detector of side length 200 cm with zero elevation is simulated and the flux as a function of position at different exposure times, 100 s, 1000 s, 5000 s respectively, are presented in Figure 5.4. This setup is the most basic setup and serves as a starting point for various AM applications.

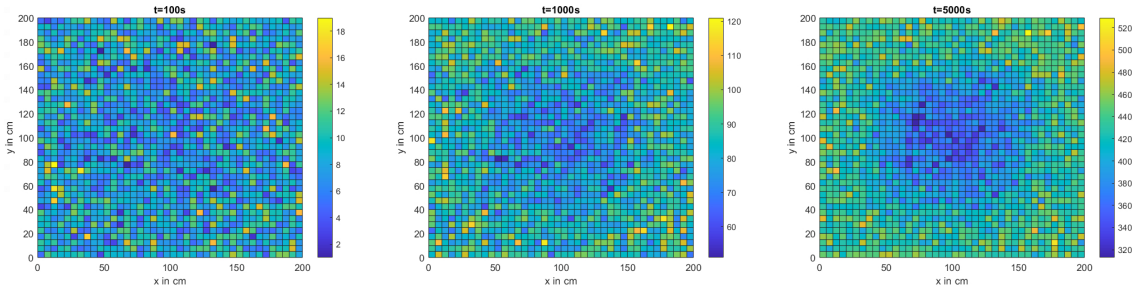

Figure 5.4. Two dimensional flux density at different exposure times.

Even with a relatively thick lead block, this setup performs poorly at detecting the boundaries of the block and provides no height (or density) information as stated earlier.

5.3.2. Column Depth Calculation with Two Upstream and Two Downstream Detectors

This setup is the most advanced setup that provides two-dimensional column depth mapping of the object. Both the downstream and upstream detector pairs (Figure 5.5) acquire the positional and angular information of the muons that reach them and the muon fluxes, $N_{up}(x, y, \theta, \phi)$ and $N_{down}(x, y, \theta, \phi)$, can be calculated. If the number of muons detected is large enough or equivalently the exposure time is long enough, from the ratio of the fluxes, and using the energy spectrum of the muon flux, the energy limit below which the muons do not reach the downstream detector pair can be found and the corresponding range can be calculated.

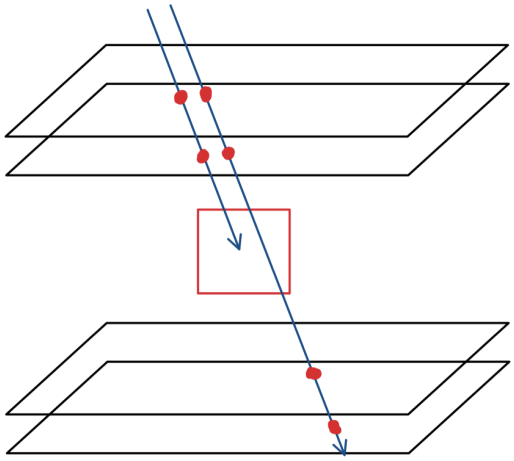

Figure 5.5. Detector setup 2. For demonstration purposes the object and the detector pairs are drawn with a separation. There is no separation in the actual simulation setup.

The same lead block and detector geometry previously used is used again. The height of the object is the known parameter and density of the object is calculated using the fluxes $N_{up}(x, y, \theta, \phi)$ and $N_{down}(x, y, \theta, \phi)$ as follows. From the ratio of the fluxes and the muon energy spectrum (Figure 3.3), the energy below which the muons are "absorbed" is found. Then the corresponding column depth and density is computed. The simulation results are shown in Figure 5.6.

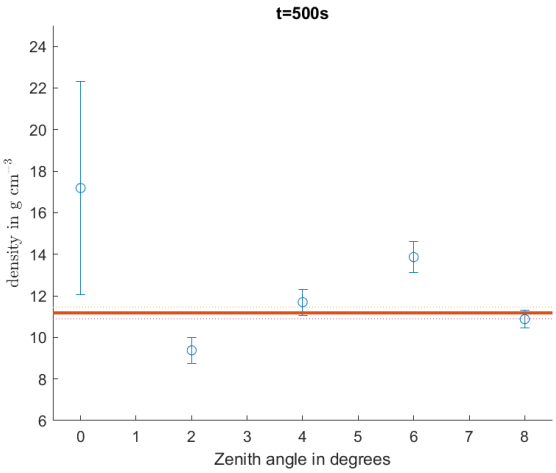

(a) Best fit density is 11.18±0.28 g cm^{-3}.

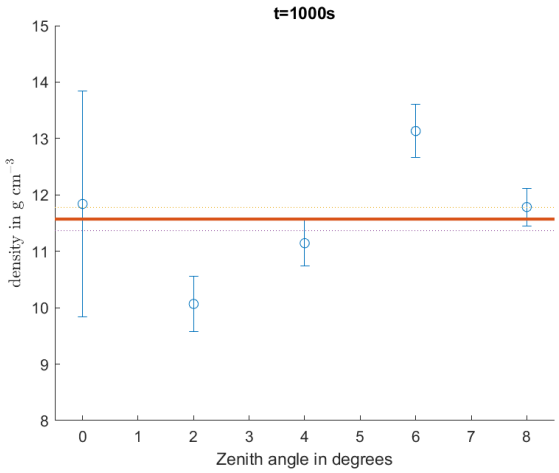

(b) Best fit density is 11.57±0.20 g cm^{-3}.

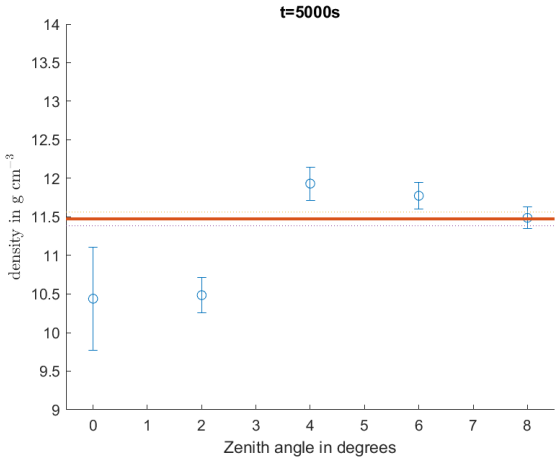

(c) Best fit density is 11.47±0.09 g cm^{-3}

Figure 5.6. Simulation results of the second setup at different exposure times. Each point corresponds to density results for zenith angles given ±1° except for 0° zenith angle where it is only +1°. Error bars are calculated assuming a pure Binomial process. Thick line is the best fit and the dotted lines are ±1σ envelopes. The true density value is 11.35 g cm^{-3}.

5.3.3. Column Depth Calculation with Two Downstream Detectors

This setup is an intermediate setup which has advantages over the first setup as it can acquire the directional information of the muon flux but is at a disadvantage compared to the second setup as it does not have the upstream pair of detectors (Figure 5.7) which supplies the information of the flux before the particles traverse the object. Therefore, the simulation program needs to compare the downstream flux with either the free sky flux or the flux away from the object.

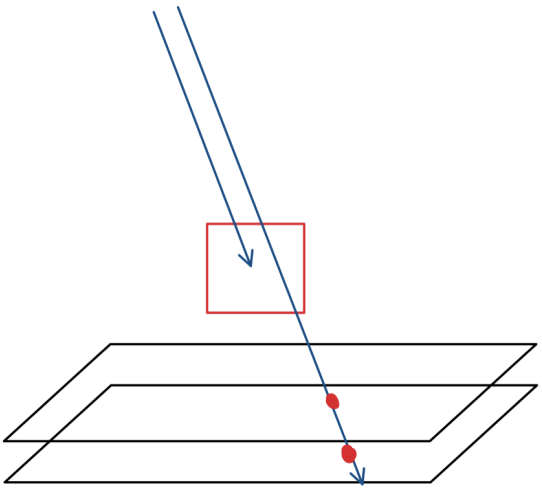

Figure 5.7. Detector setup 3

Simulation studies of this setup are performed employing the second approach of using the flux away from the object as a comparison flux. Results can be seen in Figure 5.8. Note that the results acquired with this setup are very similar to those acquired with setup 2 except at the lowest exposure time 500 s where the statistics are arguably not high enough.

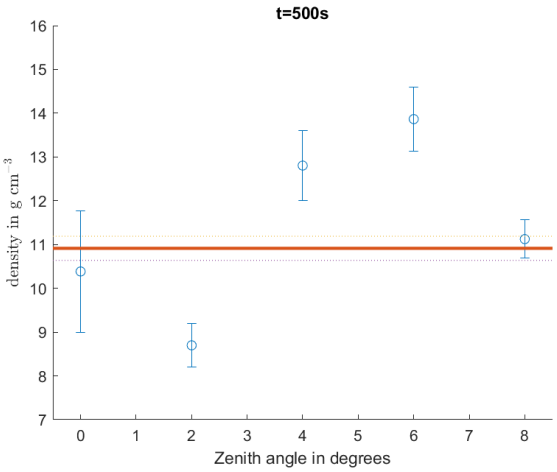

(a) Best fit density is 10.91±0.28 g cm^{-3}.

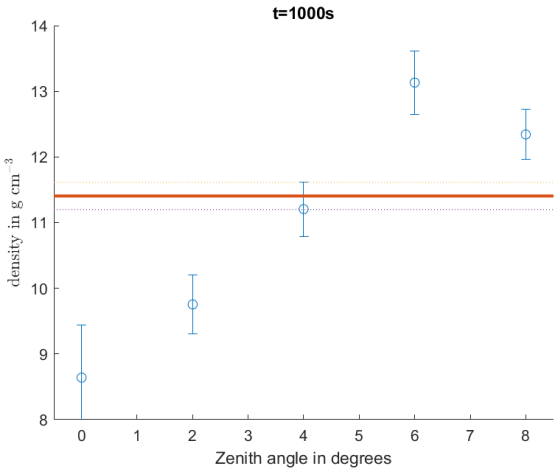

(b) Best fit density is 11.40±0.21 g cm^{-3}.

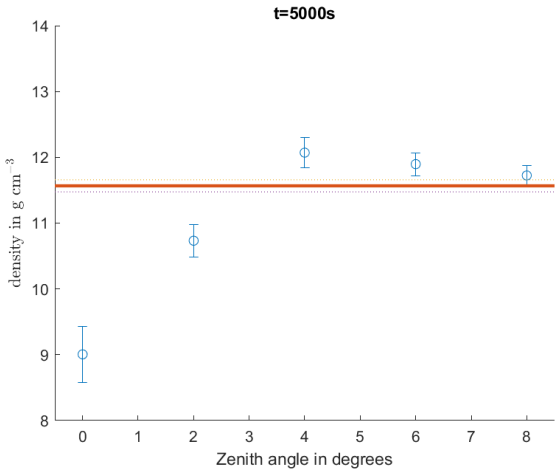

(c) Best fit density is 11.57±0.09 g cm^{-3}

Figure 5.8. Simulation results of the third setup at different exposure times. Each point corresponds to density results for zenith angles given ±1° except for 0° zenith angle where it is only +1°. Error bars are calculated assuming a pure Binomial process. Thick line is the best fit and the dotted lines are ±1σ envelopes. The true density value is 11.35 g cm^{-3}.

5.4. Simulation Results with Resistive Plate Chambers

Particle detectors widely used today are designed to operate at very high rates that are achieved by very high luminosity accelerators. AM technique, however, relies on the cosmic rays to produce the atmospheric muons with a flux of approximately 1 muon per minute per 1 cm^2 area at sea level [13]. Even with a large detection area, the rates are minuscule compared to the rates most of the detectors are capable of operating at. Therefore, rate capabilities and time resolutions, which can be explained with a similar line of reasoning, of the detectors used do not play a significant role in AM.

Apart from the physical requirements specific to the use case, the main factor is the spatial resolution [13]. As mentioned earlier, AM is efficient in detecting large objects, that might be hundreds of meters away from the detector setup. Therefore, good spatial resolution is required in order to measure the arriving angles and reconstruct the trajectories precisely. In Figures 5.9, 5.10, 5.11, the simulation results of detector setups consisting of two upstream and two downstream RPCs with varying spatial resolutions of 0.5 mm, 1 mm and 2 mm can be seen. To incorporate the effect of positional uncertainty, when calculating the angles, hence the trajectories, of each muon, the hit positions are binned and instead of using the exact positions, these binned positions are used.

In the results given, the gap between the detectors has been set to 10 cm considering two factors. As we increase the distance between the detectors, same spatial uncertainty yields less angular uncertainty hence the precision is increased. However, the trade-off is that some of the muons might be lost in the region between the detectors, which not only decreases the number of data collected and increases the exposure time required, but also makes the setup prone to bias towards detecting higher energy muons sacrificing the accuracy.

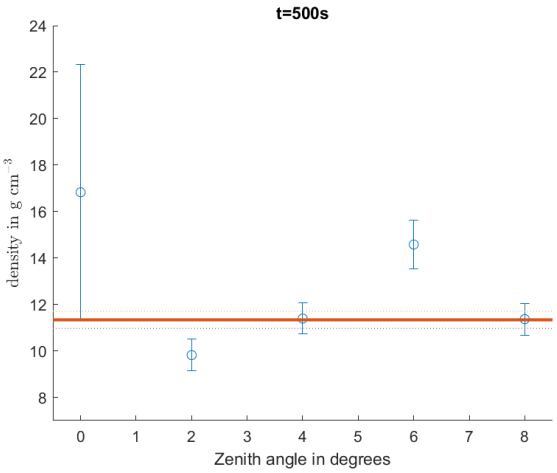

(a) Results for 0.5 mm spatial resolution and 500 s exposure time. Best fit density is 11.34±0.37 g cm^{-3}.

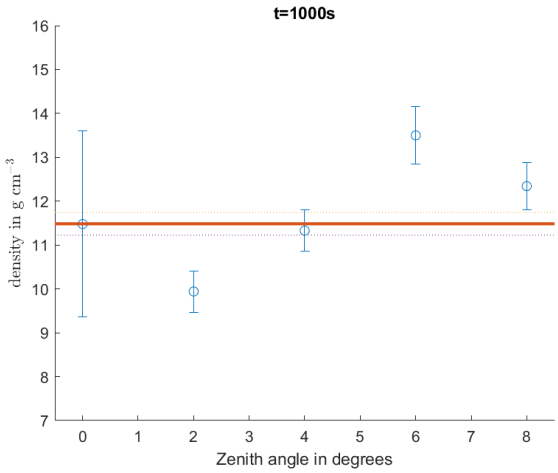

(b) Results for 0.5 mm spatial resolution and 1000 s exposure time. Best fit density is 11.48±0.26 g cm^{-3}.

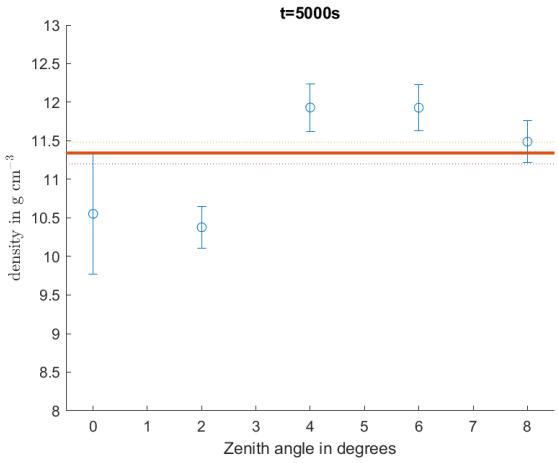

(c) Results for 0.5 mm spatial resolution and 5000 s exposure time. Best fit density is 11.34±0.14 g cm^{-3}.

Figure 5.9. Simulation results for 0.5 mm spatial resolution RPC at different exposure times. Error bars are calculated assuming a pure Binomial process. The true density is 11.35 g cm^{-3}.

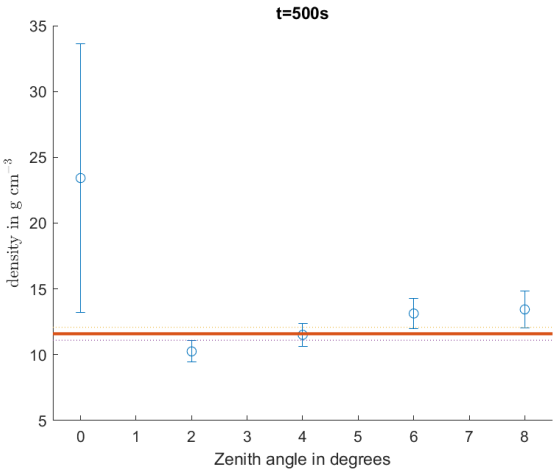

(a) Results for 1 mm spatial resolution and 500 s exposure time. Best fit density is 11.59±0.49 g cm^{-3}.

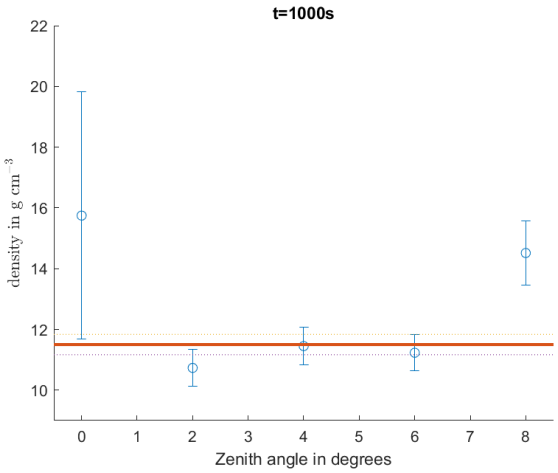

(b) Results for 1 mm spatial resolution and 1000 s exposure time. Best fit density is 11.50±0.33 g cm^{-3}.

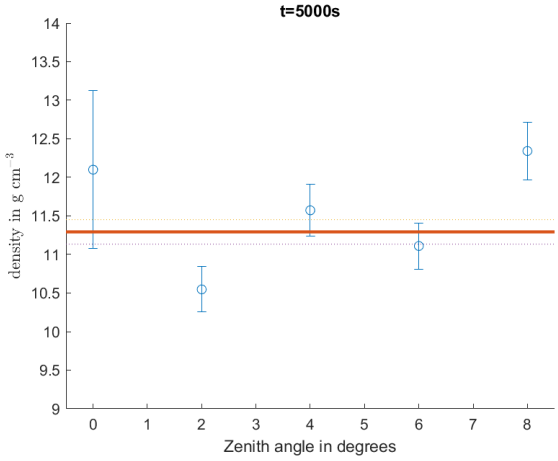

(c) Results for 1 mm spatial resolution and 5000 s exposure time. Best fit density is 11.29±0.16 g cm^{-3}.

Figure 5.10. Simulation results for 1 mm spatial resolution RPC at different exposure times. Error bars are calculated assuming a pure Binomial process. The true density is 11.35 g cm^{-3}.

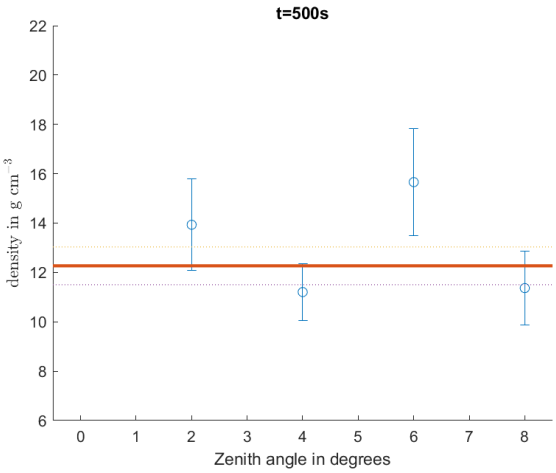

(a) Results for 2 mm spatial resolution and 500 s exposure time. Best fit density is 12.27±0.76 g cm^{-3}.

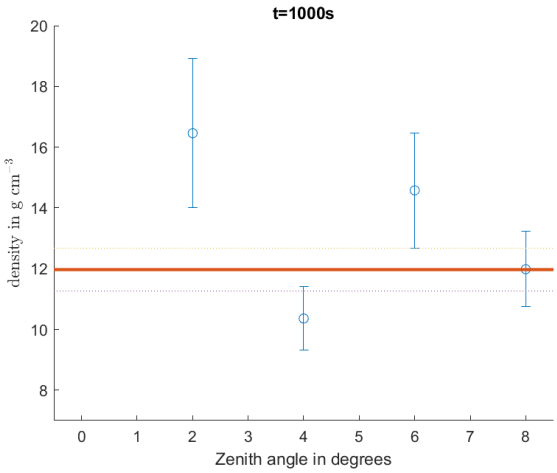

(b) Results for 2 mm spatial resolution and 1000 s exposure time. Best fit density is 11.97±0.70 g cm^{-3}.

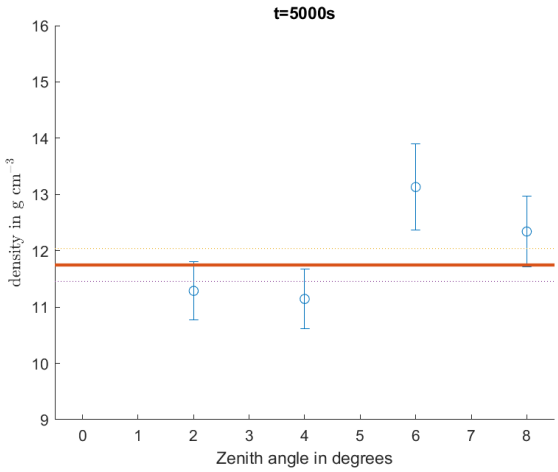

(c) Results for 2 mm spatial resolution and 5000 s exposure time. Best fit density is 11.75±0.29 g cm^{-3}.

Figure 5.11. Simulation results for 2 mm spatial resolution RPC at different exposure times. Error bars are calculated assuming a pure Binomial process. The true density is 11.35 g cm^{-3}.

6. CONCLUSION

Ever since their discovery, muons have played a crucial role in experimental particle physics and their detection has an utmost importance in various particle physics experiments. Therefore, significant effort is poured into the research and development studies of muon detectors. RPCs are currently used by many experiments and are among the strong candidates to be used in future international and domestic projects. A recent pioneering work has been done to build a domestic prototype RPC at KAHVE-Lab and the preliminary results have been promising. As the next step, in this thesis, simulations have been performed testing the design parameters of the prototype RPC as well as assessing the usability of an alternative, inexpensive, gas mixture. The results are in agreement with the literature [7].

Our work provides the basis for future studies to achieve more precise results by improving various simulation parameters described in the text. Once the desired precision is reached, they will be checked against the follow-up experimental results.

Muography, an imaging method based on Cosmic Rays, specifically atmospheric muons, employs two main techniques, absorption muography (AM) and scattering muography (SM). In this thesis, first, a very simple yet informative geometry and a variety of detection setups with ideal detectors have been simulated using a toy Monte Carlo program to estimate the theoretical precision and to determine the order of magnitude of the exposure time required. Then, the ideal detectors have been replaced by non-ideal detectors with spatial uncertainty. The results suggest, depending on the application specific geometry, RPCs might be utilized in AM.

To improve the precision of the simulation and to assess the practicality of RPCs as AM detectors a full Geant4 simulation must be performed with the whole geometry implemented. However, the results of this thesis suggest that an RPC with a spatial resolution of a few mm is capable of measuring the density of a metal block of height

1 m with an uncertainty of sub 10% withing several hours of exposure time.

REFERENCES

1. Yildizci, Z. S., *Design and Construction of a Prototype Resistive Plate Chamber*, Master's Thesis, Boğaziçi University, 2019.

2. Lechner, A., "Particle Interactions with Matter", *CERN Yellow Reports: School Proceedings*, Vol. 5, p. 47, 2018.

3. Tavernier, S., *Experimental Techniques in Nuclear and Particle Physics*, Springer, Heidelberg, Germany, 2010.

4. Zyla, P. A. *et al.*, "Review of Particle Physics", *Progress of Theoretical and Experimental Physics*, Vol. 2020, No. 8, p. 083C01, 2020.

5. Haino, S., T. Sanuki, K. Abe, K. Anraku, Y. Asaoka, H. Fuke, M. Imori, A. Itasaki, T. Maeno, Y. Makida and et al., "Measurements of Primary and Atmospheric Cosmic-ray Spectra with the BESS-TeV Spectrometer", *Physics Letters B*, Vol. 594, No. 1-2, p. 35–46, Jul 2004.

6. Shukla, P. and S. Sankrith, "Energy and Angular Distributions of Atmospheric Muons at the Earth", *arXiv: High Energy Physics - Phenomenology*, 2016.

7. Peskov, V., M. Abbrescia and P. Fonte, *Resistive Gaseous Detectors: Designs, Performance, and Perspectives*, John Wiley & Sons, Ltd, 04 2018.

8. Smirnov, I. B., "Modeling of Ionization Produced by Fast Charged Particles in Gases", *Nuclear Instruments and Methods in Physics Research, Section A: Accelerators, Spectrometers, Detectors and Associated Equipment*, Vol. 554, pp. 474–493, 2005.

9. Agostinelli, S. *et al.*, "GEANT4–a Simulation Toolkit", *Nuclear Instruments and Methods in Physics Research, Section A: Accelerators, Spectrometers, Detectors*

and Associated Equipment, Vol. 506, pp. 250–303, 2003.

10. "Garfield++ Simulation Toolkit", `https://garfieldpp.web.cern.ch`, accessed 04 June 2020.

11. Crotty, I., E. Cerron Zeballos, J. Lamas Valverde, D. Hatzifotiadou, M. Williams and A. Zichichi, "The Wide Gap Resistive Plate Chamber", *Nuclear Instruments and Methods in Physics Research Section A: Accelerators, Spectrometers, Detectors and Associated Equipment*, Vol. 360, No. 3, pp. 512–520, 1995.

12. Groom, D. E., N. V. Mokhov and S. I. Striganov, "Muon Stopping Power and Range Tables 10 MeV–100 TeV", *Atomic Data and Nuclear Data Tables*, Vol. 78, No. 2, pp. 183–356, 2001.

13. Bonechi, L., R. D'Alessandro and A. Giammanco, "Atmospheric Muons as an Imaging Tool", *Reviews in Physics*, Vol. 5, p. 100038, 2020.